

Article

Effect of Growth Temperature on Crystallization of $\text{Ge}_{1-x}\text{Sn}_x$ Films by Magnetron Sputtering

Hongjuan Huang^{1,2,3}, Desheng Zhao^{2,4}, Chengjian Qi⁴, Jingfa Huang⁴, Zhongming Zeng², Baoshun Zhang^{2,*} and Shulong Lu^{1,3,*}

¹ School of Nano-Tech and Nano-Bionics, University of Science and Technology of China, Hefei 230026, China

² Nano Fabrication Facility, Suzhou Institute of Nano-Tech and Nano-Bionics, Chinese Academy of Sciences (CAS), Suzhou 215123, China

³ Key Lab of Nanodevices and Applications, Suzhou Institute of Nano-Tech and Nano-Bionics, Chinese Academy of Sciences (CAS), Suzhou 215123, China

⁴ Nano Fabrication Facility, Guangdong Institute of Semiconductor Micro-Nano Manufacturing Technology, Guangdong 528200, China

* Correspondence: bszhang2006@sinano.ac.cn (B.Z.); slilu2008@sinano.ac.cn (S.L.)

Abstract: $\text{Ge}_{1-x}\text{Sn}_x$ film with Sn content (at%) as high as 13% was grown on Si (100) substrate with Ge buffer layer by magnetron sputtering epitaxy. According to the analysis of HRXRD and Raman spectrum, the quality of the $\text{Ge}_{1-x}\text{Sn}_x$ crystal was strongly dependent on the growth temperature. Among them, the GeSn (400) diffraction peak of the $\text{Ge}_{1-x}\text{Sn}_x$ film grown at 240 °C was the lowest, which is consistent with the Raman result. According to the transmission electron microscope image, some dislocations appeared at the interface between the Ge buffer layer and the Si substrate due to the large lattice mismatch, but a highly ordered atomic arrangement was observed at the interface between the Ge buffer layer and the $\text{Ge}_{1-x}\text{Sn}_x$ layer. The $\text{Ge}_{1-x}\text{Sn}_x$ film prepared by magnetron sputtering is expected to be a cost-effective fabrication method for Si-based infrared devices.

Keywords: $\text{Ge}_{1-x}\text{Sn}_x$ alloy; magnetron sputtering; growth temperature; Ge buffer



Citation: Huang, H.; Zhao, D.; Qi, C.; Huang, J.; Zeng, Z.; Zhang, B.; Lu, S. Effect of Growth Temperature on Crystallization of $\text{Ge}_{1-x}\text{Sn}_x$ Films by Magnetron Sputtering. *Crystals* **2022**, *12*, 1810. <https://doi.org/10.3390/cryst12121810>

Academic Editors: Francisco M. Morales, Yukun Zhao, Zhenhuan Tian and Jianya Zhang

Received: 16 November 2022

Accepted: 8 December 2022

Published: 12 December 2022

Publisher's Note: MDPI stays neutral with regard to jurisdictional claims in published maps and institutional affiliations.



Copyright: © 2022 by the authors. Licensee MDPI, Basel, Switzerland. This article is an open access article distributed under the terms and conditions of the Creative Commons Attribution (CC BY) license (<https://creativecommons.org/licenses/by/4.0/>).

1. Introduction

$\text{Ge}_{1-x}\text{Sn}_x$ alloys have attracted considerable attention in Si-based optoelectronic device integration because of their enhanced carrier mobility, adjustable band gap structure and compatibility with the CMOS processes [1–5]. Efficient devices based on $\text{Ge}_{1-x}\text{Sn}_x$ have been fabricated, including thin film transistors [6–9], solar cells [10], photodetectors [11–13], LEDs [14–17], lasers [18,19], etc. By adjusting the content of Sn and the strain of $\text{Ge}_{1-x}\text{Sn}_x$, the direct band gap can be extended to mid-infrared applications [20–22]. However, there are some difficulties in preparing $\text{Ge}_{1-x}\text{Sn}_x$ alloys with high Sn content and good crystal quality on a Si substrate [23,24]. At first, the equilibrium solid solubility of Sn in Ge is as low as about 0.5% [25]. Secondly, the phenomenon of Sn segregation easily appears during fabrication. Thirdly, the lattice mismatch between Ge and α -Sn is about 14.7% [26]. Thus, determining how to achieve a high Sn content and good quality $\text{Ge}_{1-x}\text{Sn}_x$ alloy is critical for fabricating high-performance $\text{Ge}_{1-x}\text{Sn}_x$ photoelectronic devices.

So far, researchers have successfully prepared $\text{Ge}_{1-x}\text{Sn}_x$ alloy films using molecular beam epitaxy (MBE) [27–29], chemical vapor deposition (CVD) [30–32], magnetron sputtering [33–36] and solid phase crystallization [37,38]. Among these methods, MBE is a method that can accurately control the thickness and structure of thin films. However, once the layer thickness exceeds the critical thickness [39,40], the screw dislocation begins to appear, which is caused by lattice mismatch, thus affecting the crystal quality of the material. CVD can release misfit dislocations at the interface rather than forming through dislocations, so the thin film materials epitaxy by this technology have perfect crystal quality [41–43]. Magnetron sputtering is a low-cost and feasible method for $\text{Ge}_{1-x}\text{Sn}_x$ mass production.

Qian, L. et al. used Ge (100) and GaAs (100) substrates with high lattice matching to obtain a $\text{Ge}_{1-x}\text{Sn}_x$ layer with good crystal quality by sputtering [44–46]. Grant, J. et al. adopted a CMOS compatible Si (100) substrate, and the $\text{Ge}_{1-x}\text{Sn}_x$ layer obtained by sputtering was polycrystalline [34,47,48]. There are few published papers about obtaining single crystal $\text{Ge}_{1-x}\text{Sn}_x$ on silicon substrate by sputtering. Zheng Jun et al. [24] realized $\text{Ge}_{1-x}\text{Sn}_x$ single crystal film with low Sn content on Ge/Si (100) substrate, in which Ge was the buffer layer, the deposition temperature was 400 °C, the deposition temperature of $\text{Ge}_{1-x}\text{Sn}_x$ films was 150 °C, and the highest Sn content was 0.06. Tsukamoto, T. et al. [49] deposited single crystal $\text{Ge}_{1-x}\text{Sn}_x$ film with x of about 0.115 on Si (100) substrate by magnetron sputtering without a buffer layer, and the deposition temperature was 250 °C. At present, single crystal $\text{Ge}_{1-x}\text{Sn}_x$ alloy films deposited on Si (100) substrate by epitaxial sputtering have the problems of many dislocations and low Sn doping, and the highest Sn doping is 0.115 [26,49,50]. Generally, when x is greater than 0.1, the energy band of $\text{Ge}_{1-x}\text{Sn}_x$ will be transformed into a direct band gap, so it is necessary to further increase the Sn content of single crystal $\text{Ge}_{1-x}\text{Sn}_x$ grown on silicon substrate by sputtering.

In this paper, we report the growth of $\text{Ge}_{1-x}\text{Sn}_x$ crystalline films on Si (100) substrates by sputtering. We have studied the possibility of growing single crystal $\text{Ge}_{1-x}\text{Sn}_x$ with Sn content more than 10% on Ge buffer layer. The Ge buffer layer was deposited at 300 °C, with a thickness of 572 nm. By adjusting the deposition temperature of $\text{Ge}_{1-x}\text{Sn}_x$ at 180–300 °C, single crystal $\text{Ge}_{1-x}\text{Sn}_x$ alloy films were obtained in which the highest Sn content (at%) reached 13%.

2. Materials and Methods

$\text{Ge}_{1-x}\text{Sn}_x$ epitaxial layers were deposited in a physical vapor deposition (PVD) system manufactured by ULVAC Corporation. Figure 1 is a schematic diagram of $\text{Ge}_{1-x}\text{Sn}_x$ deposition, in which Ge target and Sn target are installed at different target positions and sputtered at the same time. The substrate was placed on the bottom sample table, which can rotate horizontally and move up and down and heat. The sputtering rate of thin film was determined by sputtering power, sputtering distance, etc. The film thickness was obtained by scanning electron microscope profile test. Before deposition, we cleaned and activated the surface of the silicon substrate. Firstly, it was washed with sulfuric acid ($\text{H}_2\text{SO}_4:\text{H}_2\text{O}_2 = 7:3$) solution for 10 min and washed with deionized water 10 times to remove organic and inorganic pollution. Then, it was soaked in diluted HF ($\text{HF}:\text{H}_2\text{O} = 1:10$) solution at room temperature for 30 s to remove the oxide layer on the surface. Finally, it was washed with deionized water 10 times and dried with nitrogen. The base pressure of the sputtering chamber was less than 4.0×10^{-4} Pa. Then, the substrate was quickly loaded into the growth chamber. After the vacuum degree reached 4.0×10^{-4} Pa, the substrate was heated at 300 °C for 1 h, and then the Ge buffer layer was deposited with a thickness of about 572 nm. Then, different $\text{Ge}_{1-x}\text{Sn}_x$ alloy films were deposited on the Ge buffer layer by changing the temperature of the substrate to 180 °C, 200 °C, 225 °C, 240 °C, 250 °C, 260 °C, 275 °C and 300 °C, respectively. The $\text{Ge}_{1-x}\text{Sn}_x$ film was deposited by Ge and Sn co-sputtering, and its thickness was about 350 nm. In the process of sputtering deposition, argon was filled to make the chamber pressure reach 0.4 Pa. The composition of the $\text{Ge}_{1-x}\text{Sn}_x$ films was achieved by maintaining a constant DC power of 130 W for the Ge target, and RF power of 40 W for the Sn target. The deposition rate of Ge and Sn were controlled about 1.2 Å/s, 0.22 Å/s, respectively. For comparison, the sample with only a Ge buffer layer was deposited under the same conditions as the samples with $\text{Ge}_{1-x}\text{Sn}_x$ alloy film.

The properties of the Ge buffer layer and the GeSn thin film were tested and analyzed by high-resolution X-ray diffraction (HR-XRD, X'pert PRO, PANalytical, Suzhou, China), Raman scattering (Raman, Labram HR 800, HORIBA Jobin Yvon, Suzhou, China), atomic force microscope (AFM, Dimension ICON, Bruker, Suzhou, China) and high-resolution transmission electron microscope (HRTEM, Talos F200X, Thermo Fisher Scientific, Suzhou, China). Among them, HR-XRD measured the 2θ - ω diffraction peaks of (004) and (224)

planes, with a step size of 0.05° , a time per size of 1s, and a scanning range of $60\text{--}72^\circ$ and $78\text{--}92^\circ$, respectively. It was used to study the crystallization quality of single crystal films and calculate the Sn content according to the diffraction peak position and other information. A Raman scattering experiment was carried out at room temperature, the spectral line was 532 nm, exposure time was 5 s, the accumulation numbers were twice, and the scanning range was $200\text{--}350\text{ cm}^{-1}$. It was used to characterize the crystal quality and Sn composition of $\text{Ge}_{1-x}\text{Sn}_x$ film on the surface. AFM was used to characterize the surface roughness and morphology of $\text{Ge}_{1-x}\text{Sn}_x$ thin films in tapping mode with a scanning range of $5\text{ }\mu\text{m} \times 5\text{ }\mu\text{m}$, and to analyze the crystal particle size and morphology of the films. The working voltage of HRTEM is 200 kV. By observing the (110) surface of the sample, the atomic-scale material properties such as the lattice matching between materials, the crystal quality of single-layer materials and the composition ratio of alloy films could be analyzed.

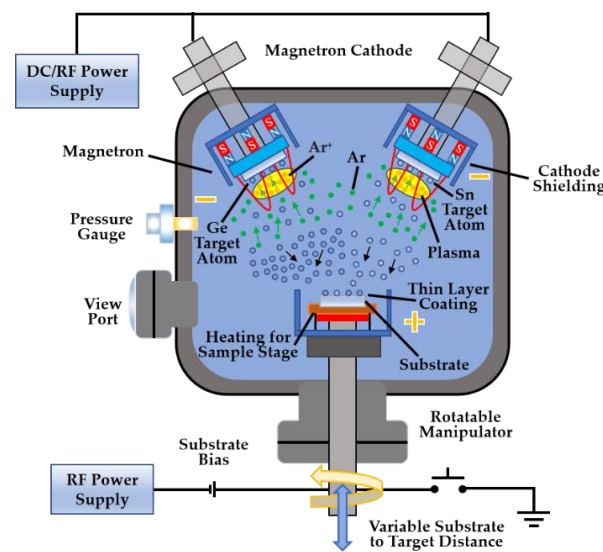


Figure 1. $\text{Ge}_{1-x}\text{Sn}_x$ co-sputtering schematic diagram.

Table 1 shows the parameters of the $\text{Ge}_{1-x}\text{Sn}_x$ samples, such as out-of-plane (α_{\perp}) lattice constants, in-plane (α_{\parallel}) lattice constants, unstrained lattice constants (α_0), measured Sn content (x_m), degree of strain relaxation (R) and in-plane strain (ϵ_{\parallel}). These parameters were calculated according to the HRXRD test results. According to Bragg's law, the out-of-plane and in-plane lattice constants of the $\text{Ge}_{1-x}\text{Sn}_x$ layers were extracted from the positions of the peaks of GeSn (004) and GeSn (224), which are given by:

$$\alpha_{\perp} = \frac{2\lambda}{\sin \theta_{004}} \quad (1)$$

$$\alpha_{\parallel} = \frac{\sqrt{2}\lambda}{\sqrt{\sin^2 \theta_{224} - \sin^2 \theta_{004}}} \quad (2)$$

Table 1. Out-of-plane (α_{\perp}) lattice constants, in-plane (α_{\parallel}) lattice constants, unstrained lattice constants (α_0), measured Sn content (x_m), degree of strain relaxation (R) and in-plane strain (ϵ_{\parallel}) of the $\text{Ge}_{1-x}\text{Sn}_x$ samples.

Growth Temperature ($^\circ\text{C}$)	α_{\perp} (nm)	α_{\parallel} (nm)	α_0 (nm)	x_m (%)	R (%)	ϵ_{\parallel} (%)
180	0.57702	0.56998	0.57399	9.98	41.1	-0.007
200	0.57676	0.56990	0.57381	10.25	40.9	-0.007
225	0.57860	0.57688	0.57786	14.29	91	-0.002
240	0.57871	0.57738	0.57813	15.38	93.2	-0.001
250	0.57826	0.57616	0.57735	13.79	88.2	-0.002

Then, the Sn composition of $\text{Ge}_{1-x}\text{Sn}_x$ layers could be calculated by simultaneously solving the Vegard's law and the Poisson's relationship, in which the bowing parameter of 0.004 nm in the Vegard's law was considered [51], and the elastic constants of $\text{Ge}_{1-x}\text{Sn}_x$ layers in Poisson's relationship was obtained by the linear interpolation of Ge and Sn. The R and ε_{\parallel} were calculated according to the following equation:

$$\alpha_0 = \frac{\alpha_{\perp} + \frac{2C_{12}}{C_{11}}\alpha_{\parallel}}{1 + \frac{2C_{12}}{C_{11}}} = \alpha_{\text{Ge}}(1-x) + \alpha_{\text{Sn}}x + bx(1-x) \quad (3)$$

$$R = \frac{\alpha_{\parallel} - \alpha_{\text{sub}}}{\alpha_0 - \alpha_{\text{sub}}} \quad (4)$$

$$\varepsilon_{\parallel} = \frac{\alpha_{\parallel} - \alpha_0}{\alpha_0} \quad (5)$$

where α_{sub} and α_0 are the lattice constants of the Ge Buffer and unstrained $\text{Ge}_{1-x}\text{Sn}_x$ layer, respectively.

As can be seen from Table 1, the content of Sn in the $\text{Ge}_{1-x}\text{Sn}_x$ film deposited at 240 °C is the highest, with the calculated value of 15.38%, which is 0.02 larger than the EDX test result of 13%, and the strain relaxation degree is also the highest, with the value of 93.2. The in-plane strain results show that all $\text{Ge}_{1-x}\text{Sn}_x$ films have small compressive stress, and the strain of $\text{Ge}_{1-x}\text{Sn}_x$ deposited at 240 °C is the largest. The results show that the unstrained lattice constant and stress increase with the increase of Sn content.

The Ge–Ge LO Raman peak ($\omega_{\text{Ge-Ge}}$) of $\text{Ge}_{1-x}\text{Sn}_x$ can be influenced by the Sn composition (x) and in-plane strain (ε_{\parallel}) as:

$$\omega_{\text{Ge-Ge}} = \omega_0 + ax + b\varepsilon_{\parallel} \quad (6)$$

where ω_0 is the bulk Ge Raman frequency at 301 cm^{-1} , and the coefficients a and b are chosen as -95.1 and -435.6 cm^{-1} , respectively [52,53]. According to the EDX test, the Sn content of the sample grown at 240 °C is about 13%, and the calculated Ge–Ge is 288.2 cm^{-1} , which is close to the Raman measurement value of 287.5 cm^{-1} .

3. Results and Discussion

Figure 2 shows the X-ray diffractograms of the $\text{Ge}_{1-x}\text{Sn}_x$ films deposited on buffered Ge layers in different conditions. The (004) and (224) plane XRD diffraction peaks of Si, Ge and GeSn are obvious in Figure 2. When the deposition temperature is between 180–250 °C, there is a diffraction peak of GeSn. This shows that the $\text{Ge}_{1-x}\text{Sn}_x$ alloy films under these process conditions are single crystal films. With the increase of deposition temperature, the diffraction peak intensity of $\text{Ge}_{1-x}\text{Sn}_x$ increases, and the position of diffraction peak decreases. At 240 °C, the intensity of the diffraction peak is the highest, and the position of the diffraction peak is the lowest, which indicates that the preferred orientation of $\text{Ge}_{1-x}\text{Sn}_x$ thin film crystal grown under this condition is obvious, and the Sn content is the highest. When the temperature rises to 260–300 °C, the diffraction peak of Ge widens, which indicates that the diffraction peak position of $\text{Ge}_{1-x}\text{Sn}_x$ is close to Ge; that is, the content of Sn drops sharply.

As we all know, Raman measurement is a common surface detection technology. By analyzing the intensity, peak position change and full width at half maximum of the Raman peak, the information of material composition, strain and crystal quality of semiconductor materials can be determined. Figure 3 shows the Raman spectrum of the Ge buffer layer and the $\text{Ge}_{1-x}\text{Sn}_x$ thin films prepared at different deposition temperatures. The spectrum of the Ge buffer can be seen to consist of one strong Ge–Ge LO Raman peak at 301.87 cm^{-1} . Similarly, the spectra of the $\text{Ge}_{1-x}\text{Sn}_x$ films consists of a strong Ge–Ge LO Raman peak between 287.5 cm^{-1} and 290.6 cm^{-1} . However, with the decrease of the deposition temperature of $\text{Ge}_{1-x}\text{Sn}_x$, the Ge–Ge LO Raman peak in $\text{Ge}_{1-x}\text{Sn}_x$ alloys

gradually widens and moves to a higher wavenumber. The Ge–Ge LO Raman peak of the thin film deposited at 240 °C is the lowest, which is in consistent with the results of HRXRD.

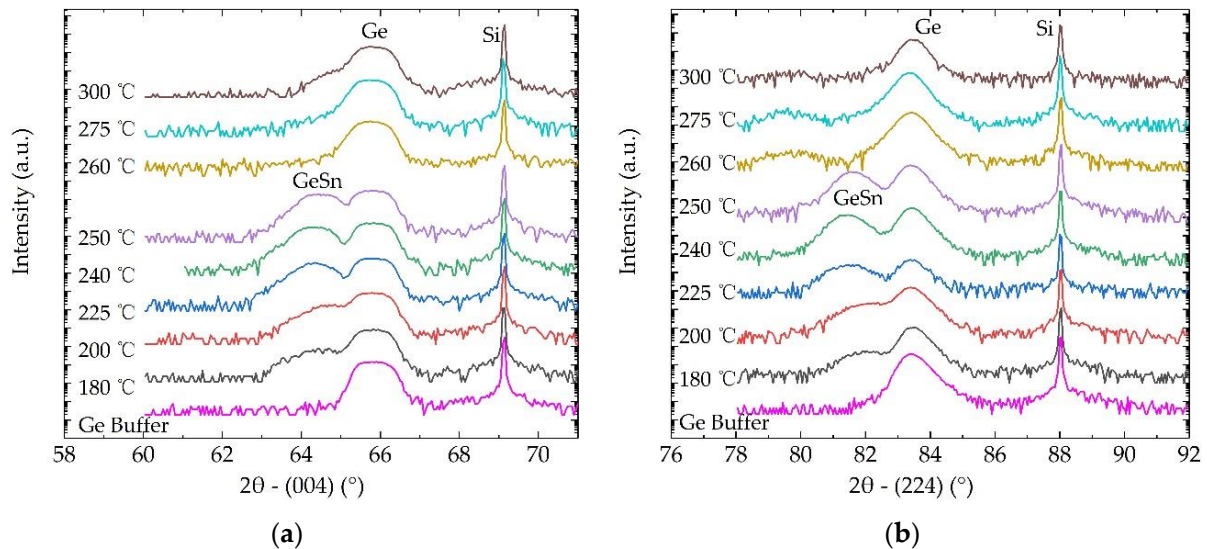


Figure 2. HR-XRD 2θ-ω scans of the $\text{Ge}_{1-x}\text{Sn}_x$ films on Si (100) for different deposited temperatures: (a) (004); (b) (224).

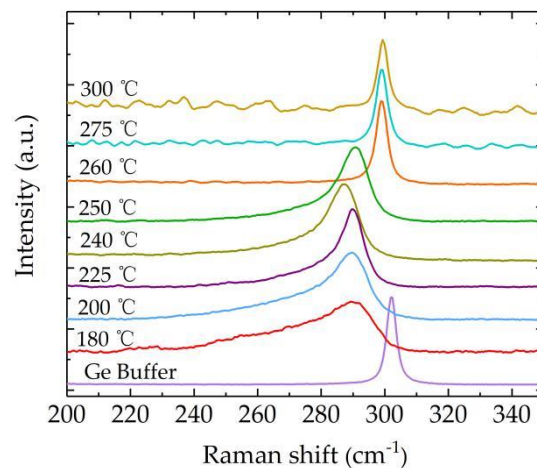


Figure 3. Ge-Ge Raman spectra of $\text{Ge}_{1-x}\text{Sn}_x$ layers with different growth temperature.

In order to determine the surface morphology of the $\text{Ge}_{1-x}\text{Sn}_x$ layer, atomic force microscopy (AFM) measurement was performed. Figure 4a–i shows the typical $5\ \mu\text{m} \times 5\ \mu\text{m}$ AFM images of the Ge Buffer layer and $\text{Ge}_{1-x}\text{Sn}_x$ layers, and the RMS (root mean square roughness) value of the $\text{Ge}_{1-x}\text{Sn}_x$ samples was extracted from AFM scans. It was found that the root mean square roughness (Rq) value of Ge Buffer was 1.21 nm and that of $\text{Ge}_{1-x}\text{Sn}_x$ samples was 4.42–41.9 nm, respectively. Figure 5 shows the comparison results of Rq values of Ge and $\text{Ge}_{1-x}\text{Sn}_x$ samples. With the increase of temperature, the roughness increases at first, decreases at 200 °C and then increases continuously. When the temperature is higher than 260 °C, the roughness increases by an order of magnitude, and the surface of the sample is silvery white and evenly distributed. It can be explained that the increase of deposition temperature intensifies the segregation of Sn; the diameter of meta-Sn particles is about 2 μm .

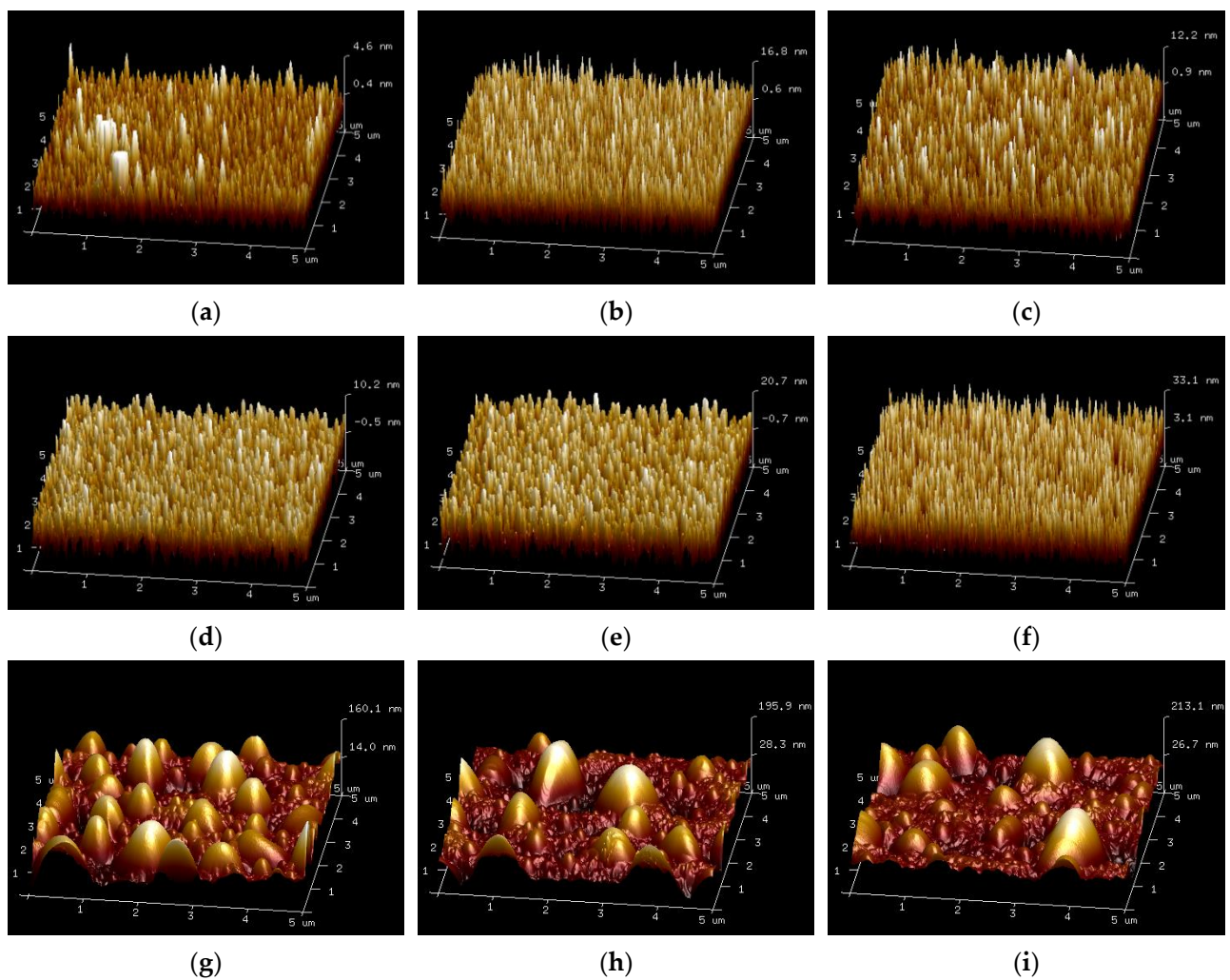


Figure 4. AFM images were obtained from the Ge buffer layer and $\text{Ge}_{1-x}\text{Sn}_x$ samples at different deposition temperatures: (a) Ge Buffer; (b) $\text{Ge}_{1-x}\text{Sn}_x$ deposited at 180 °C; (c) $\text{Ge}_{1-x}\text{Sn}_x$ deposited at 200 °C; (d) $\text{Ge}_{1-x}\text{Sn}_x$ deposited at 225 °C; (e) $\text{Ge}_{1-x}\text{Sn}_x$ deposited at 240 °C; (f) $\text{Ge}_{1-x}\text{Sn}_x$ deposited at 250 °C; (g) $\text{Ge}_{1-x}\text{Sn}_x$ deposited at 260 °C; (h) $\text{Ge}_{1-x}\text{Sn}_x$ deposited at 275 °C; (i) $\text{Ge}_{1-x}\text{Sn}_x$ deposited at 300 °C.

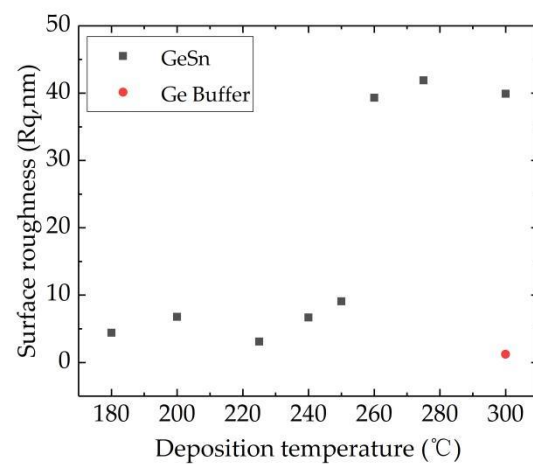


Figure 5. Comparison of surface roughness between the Ge buffer layer and $\text{Ge}_{1-x}\text{Sn}_x$ samples deposited at different temperatures.

In order to further characterize the crystallinity, XTEM measurement was carried out on the $\text{Ge}_{1-x}\text{Sn}_x$ alloy film deposited at 240 °C. As shown in Figure 6a, the interfaces between $\text{Ge}_{1-x}\text{Sn}_x$ /Ge buffer/Si substrate were clear and recognizable. Figure 6b confirms the relaxation characteristics of the Ge buffer layer and clearly proves that the threading dislocations appear in the Ge buffer layer due to the mismatch between Ge and Si. In Figure 6c, the interface between the $\text{Ge}_{1-x}\text{Sn}_x$ /Ge buffer layer, atomic observation shows a highly ordered atomic arrangement in the interface. In Figure 6d–f is fast Fourier transformation (FFT) patterns of $\text{Ge}_{1-x}\text{Sn}_x$, $\text{Ge}_{1-x}\text{Sn}_x$ /Ge buffer layer interface and Ge buffer layer. Diffraction spots are typical face-centered cubic [011] patterns, and clear lattice fringes of Ge and the $\text{Ge}_{1-x}\text{Sn}_x$ layer indicate that single-crystal films are grown by sputtering and the $\text{Ge}_{1-x}\text{Sn}_x$ layer is coherent with the Ge crystal.

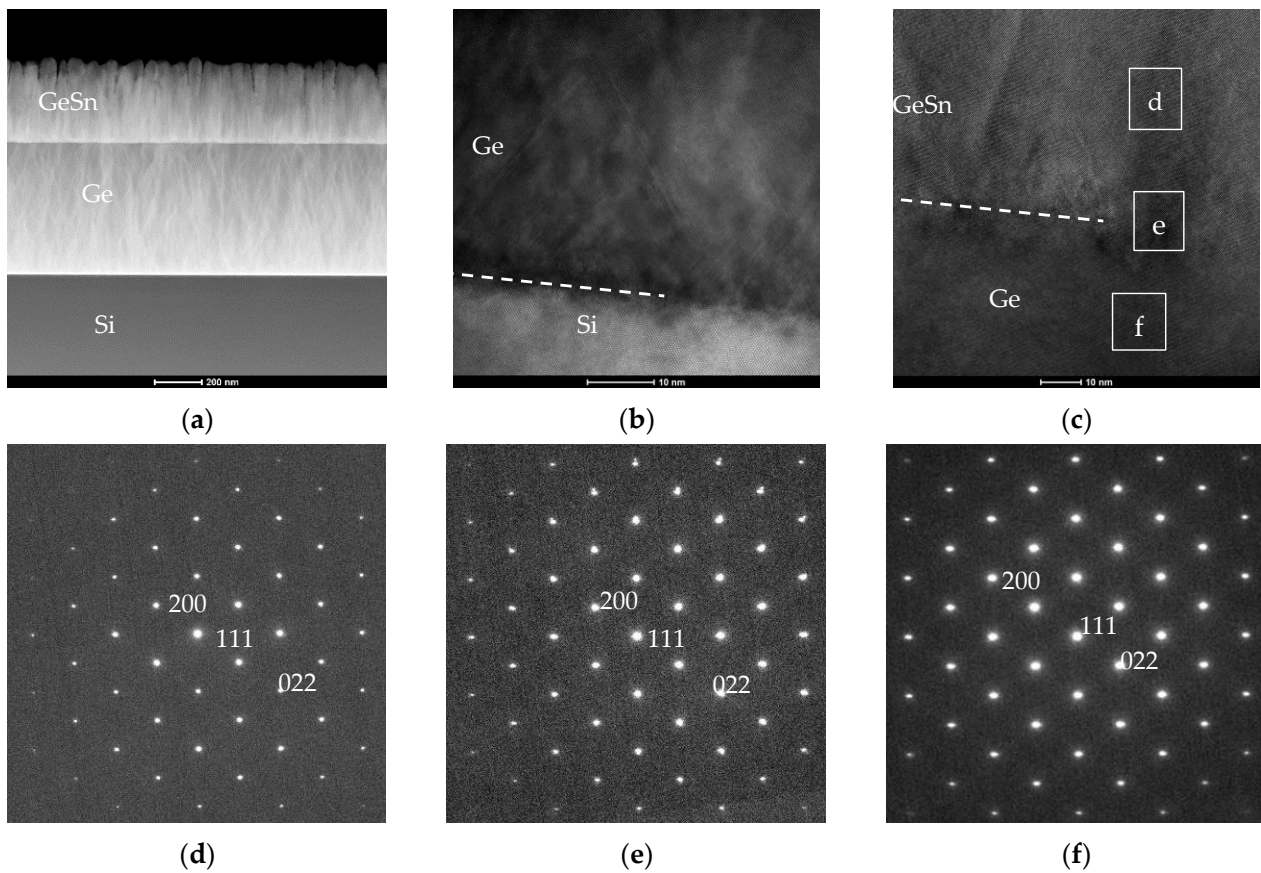


Figure 6. XTEM images of $\text{Ge}_{1-x}\text{Sn}_x$ film deposited at 240 °C: (a) full view of the film by scanning TEM; (b) high resolution TEM at Ge/Si interface; (c) high resolution TEM at Ge/ $\text{Ge}_{1-x}\text{Sn}_x$ interface; (d–f) show the FFT patterns corresponding to the various regions in (c).

Electron dispersive X-ray (EDX) spectroscopy was performed to identify the elemental composition of the Ge and $\text{Ge}_{1-x}\text{Sn}_x$ films, and the results are shown in Figure 7. Figure 7a shows a spectral scan of the concentration values of uniformly distributed Sn, Ge and Si. Figure 7b shows the line scan of the concentration values of Sn, Ge and Si, where the Sn content (at%) is about 12.6–13.06%. According to the content distribution of Sn, there is no Sn segregation on the surface of the $\text{Ge}_{1-x}\text{Sn}_x$ film. Compared with references of single crystal $\text{Ge}_{1-x}\text{Sn}_x$ deposited by magnetron sputtering on silicon substrate, the tin content is the highest in this work, and the specific data are shown in Table 2.

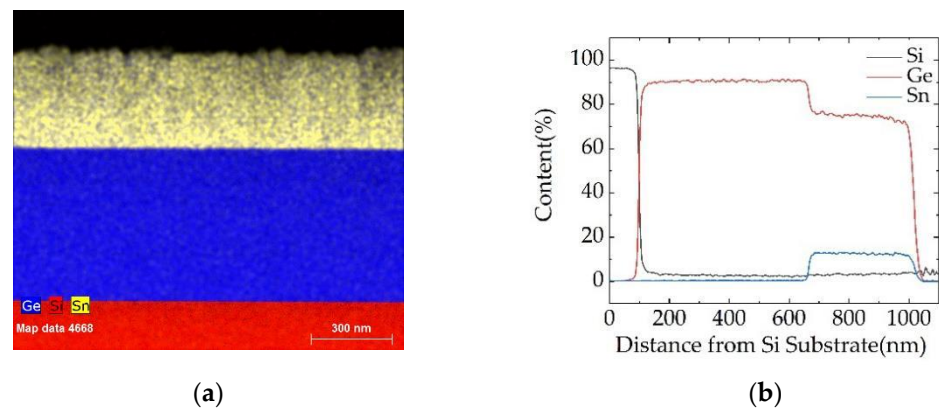


Figure 7. EDX of the sample with $\text{Ge}_{1-x}\text{Sn}_x$ film as deposited at 240°C , (a) map scanning; (b) line scanning.

Table 2. Comparison of the Sn content of crystalline $\text{Ge}_{1-x}\text{Sn}_x$ with those found in other references.

Reference	Sn Content (at%)	Buffer
[26]	6	Ge
[49]	11.5	None
[50]	3	Ge
This work	12.6–13.06	Ge

In this work, $\text{Ge}_{1-x}\text{Sn}_x$ alloy thin films were prepared by a Ge–Sn co-sputtering principle, and the Ge target and Sn target were mounted on two targets, respectively. The sputtering power of Ge and Sn was controlled to achieve different atomic ratios of Sn. The temperature of the substrate can be adjusted. The higher the temperature, the higher the mobility energy of Sn atoms, and the easier it is to move to the appropriate position. Therefore, with the increase of temperature, Sn atoms occupied the position of Ge atoms forming a $\text{Ge}_{1-x}\text{Sn}_x$ alloy, and with the increase of temperature to 240°C , the Sn doping peak was reached. When the temperature continued to rise, segregation occurred. When the temperature rose to 260°C , segregation intensified, Sn atoms migrated to the surface of the sample, and the Sn content of $\text{Ge}_{1-x}\text{Sn}_x$ alloy decreased.

4. Conclusions

In this paper, the structural characteristics of $\text{Ge}_{1-x}\text{Sn}_x$ thin films at different substrate temperatures were studied in detail. XRD, Raman, TEM and AFM analysis showed that the coherent growth of $\text{Ge}_{1-x}\text{Sn}_x$ and Ge can be achieved by adjusting the substrate temperature, and the Sn content in the $\text{Ge}_{1-x}\text{Sn}_x$ film deposited at 240°C was the highest, with the Sn content (at%) reaching 13%. These results show that single crystal $\text{Ge}_{1-x}\text{Sn}_x$ films can be grown on Si (001) wafer by sputtering at a temperature near the melting point of Sn, and its Sn content is the highest among GeSn prepared by sputtering on Si (001) substrate reported at present.

Author Contributions: Conceptualization, H.H., S.L., B.Z. and Z.Z.; methodology, H.H., S.L., B.Z. and Z.Z.; formal analysis, C.Q., J.H. and H.H.; visualization, C.Q., J.H. and H.H.; investigation, C.Q.; writing—original draft preparation, H.H.; writing—review and editing, H.H., D.Z. and S.L.; supervision, S.L.; project administration, S.L.; funding acquisition, S.L. All authors have read and agreed to the published version of the manuscript.

Funding: This research was funded by National Key R&D Program, grant number 2018YFB2003305.

Data Availability Statement: The data presented in this study are available within the manuscript.

Acknowledgments: The authors thank Platform for Characterization & Test of Suzhou Institute of Nano-Tech and Nano-Bionics (SINANANO), Chinese Academy of Sciences (CAS) for the technical support.

Conflicts of Interest: The authors declare no conflict of interest.

References

1. Tsai, C.H.; Lin, K.C.; Cheng, C.Y.; Lee, K.C.; Cheng, H.H.; Chang, G.E. GeSn lateral p-i-n waveguide photodetectors for mid-infrared integrated photonics. *Opt. Lett.* **2021**, *46*, 864–867. [[CrossRef](#)] [[PubMed](#)]
2. Buzynin, Y.N.; Shengurov, V.G.; Denisov, S.A.; Yunin, P.A.; Chalkov, V.Y.; Drozdov, M.N.; Korolyov, S.A.; Nezhdanov, A.V. High Hole Mobility of Polycrystalline GeSn Layers Grown by Hot-Wire Chemical Vapor Deposition on Diamond Substrates. *Phys. Status Solidi-Rapid Res. Lett.* **2022**, *16*, 2100421. [[CrossRef](#)]
3. Moto, K.; Yoshimine, R.; Suemasu, T.; Toko, K. Improving carrier mobility of polycrystalline Ge by Sn doping. *Sci. Rep.* **2018**, *8*, 14832. [[CrossRef](#)] [[PubMed](#)]
4. Sau, J.D.; Cohen, M.L. Possibility of increased mobility in Ge-Sn alloy system. *Phys. Rev. B* **2007**, *75*, 045208. [[CrossRef](#)]
5. Anas, E.; Dan, B.; Nils, V.D.D.; Konstantinos, P.; Gilles, P.; Nicolas, Z.; Etienne, H.; Xavier, C.; Sébastien, S.; Isabelle, S.; et al. Ultra-low-threshold continuous-wave and pulsed lasing in tensile-strained GeSn alloys. *Nat. Photonics* **2020**, *14*, 375–382.
6. Uchida, N.; Hattori, J.; Lieten, R.R.; Ohishi, Y.; Takase, R.; Ishimaru, M.; Fukuda, K.; Maeda, T.; Locquet, J.P. Carrier and heat transport properties of poly-crystalline GeSn films for thin-film transistor applications. *J. Appl. Phys.* **2019**, *126*, 145105. [[CrossRef](#)]
7. Zhang, L.; Hong, H.Y.; Yu, C.Y.; Li, C.; Chen, S.Y.; Huang, W.; Wang, J.Y.; Wang, H. Poly-GeSn Junctionless Thin-Film Transistors on Insulators Fabricated at Low Temperatures via Pulsed Laser Annealing. *Phys. Status Solidi-Rapid Res. Lett.* **2019**, *13*, 1900420. [[CrossRef](#)]
8. Moto, K.; Yamamoto, K.; Imajo, T.; Suemasu, T.; Nakashima, H.; Toko, K. Sn Concentration Effects on Polycrystalline GeSn Thin Film Transistors. *IEEE Electron Device Lett.* **2021**, *42*, 1735–1738. [[CrossRef](#)]
9. Mizoguchi, T.; Ishiyama, T.; Moto, K.; Imajo, T.; Suemasu, T.; Toko, K. Solid-Phase Crystallization of GeSn Thin Films on GeO₂-Coated Glass. *Phys. Status Solidi-Rapid Res. Lett.* **2022**, *16*, 2100509. [[CrossRef](#)]
10. Zhu, X.M.; Cui, M.; Wang, Y.; Yu, T.J.; Li, Q.Y.; Deng, J.X.; Gao, H.L. Evaluation of electricity generation on GeSn single-junction solar cell. *Int. J. Energy Res.* **2022**, 1–8. [[CrossRef](#)]
11. Wu, S.T.; Xu, S.Q.; Zhou, H.; Jin, Y.H.; Chen, Q.M.; Huang, Y.C.; Zhang, L.; Gong, X.; Tan, C.S. High-Performance Back-Illuminated Ge_{0.92}Sn_{0.08}/Ge Multiple-Quantum-Well Photodetector on Si Platform for SWIR Detection. *IEEE J. Sel. Top. Quantum Electron.* **2022**, *28*, 1–9. [[CrossRef](#)]
12. Wang, N.; Xue, C.L.; Wan, F.S.; Zhao, Y.; Xu, G.Y.; Liu, Z.; Zheng, J.; Zuo, Y.H.; Cheng, B.W.; Wang, Q.M. High-Performance GeSn Photodetector Covering All Telecommunication Bands. *IEEE Photonics J.* **2021**, *13*, 1–9. [[CrossRef](#)]
13. Tran, H.; Pham, T.; Margetis, J.; Zhou, Y.Y.; Dou, W.; Grant, P.C.; Grant, J.M.; Al-Kabi, S.; Sun, G.; Soref, R.A.; et al. Si-Based GeSn Photodetectors toward Mid-Infrared Imaging Applications. *ACS Photonics* **2019**, *6*, 2807–2815. [[CrossRef](#)]
14. Zhang, L.F.; Shu, B.; Jiang, R.H.; Gao, Y.L.; Zhang, H.M.; Xuan, R.X.; Hu, H.Y. Short wave infrared LEDs based on strained GeSn. *Micro Opt. Tech Lett.* **2018**, *60*, 1151–1154. [[CrossRef](#)]
15. Oehme, M.; Werner, J.; Gollhofer, M.; Schmid, M.; Kaschel, M.; Kasper, E.; Schulze, J. Room-Temperature Electroluminescence from GeSn Light-Emitting Pin Diodes on Si. *IEEE Photonics Technol. Lett.* **2011**, *23*, 1751–1753. [[CrossRef](#)]
16. Zhou, Y.Y.; Dou, W.; Du, W.; Pham, T.; Ghetmiri, S.A.; Al-Kabi, S.; Mosleh, A.; Alher, M.; Margetis, J.; Tolle, J.; et al. Systematic study of GeSn heterostructure-based light-emitting diodes towards mid-infrared applications. *J. Appl. Phys.* **2016**, *120*, 023102. [[CrossRef](#)]
17. Chang, C.; Li, H.; Huang, S.H.; Lin, L.C.; Cheng, H.H. Temperature-dependent electroluminescence from GeSn heterojunction light-emitting diode on Si substrate. *Jpn. J. Appl. Phys.* **2016**, *55*, 04EH03. [[CrossRef](#)]
18. Kim, Y.; Assali, S.; Burt, D.; Jung, Y.; Joo, H.J.; Chen, M.; Ikonc, Z.; Moutanabbir, O.; Nam, D. Enhanced GeSn Microdisk Lasers Directly Released on Si. *Adv. Opt. Mater.* **2022**, *10*, 2101213. [[CrossRef](#)]
19. Margetis, J.; Al-Kabi, S.; Du, W.; Dou, W.; Zhou, Y.Y.; Pham, T.; Grant, P.; Ghetmiri, S.; Mosleh, A.; Li, B.H.; et al. Si-Based GeSn Lasers with Wavelength Coverage of 2–3 μm and Operating Temperatures up to 180 K. *ACS Photonics* **2018**, *5*, 827–833. [[CrossRef](#)]
20. Chang, G.-E.; Yu, S.-Q.; Liu, J.F.; Cheng, H.-H.; Soref, R.A.; Sun, G. Achievable Performance of Uncooled Homojunction GeSn Mid-Infrared Photodetectors. *IEEE J. Sel. Top. Quantum Electron.* **2022**, *28*, 1–11. [[CrossRef](#)]
21. Kumar, H.; Basu, R. Effect of Defects on the Performance of Si-Based GeSn/Ge Mid-Infrared Phototransistors. *IEEE Sens. J.* **2021**, *21*, 5975–5982. [[CrossRef](#)]
22. Zhou, Y.Y.; Ojo, S.; Wu, C.W.; Miao, Y.H.; Tran, H.; Grant, J.M.; Abernathy, G.; Amoah, S.; Bass, J.; Salamo, G.; et al. Electrically injected GeSn lasers with peak wavelength up to 2.7 μm . *Photonics Res.* **2022**, *10*, 222–229. [[CrossRef](#)]
23. Asano, T.; Shimura, Y.; Nakatsuka, O.; Zaima, S. Influence of Sn incorporation and growth temperature on crystallinity of Ge_{1-x}Sn_x layers heteroepitaxially grown on Ge(110) substrates. *Thin Solid Film.* **2013**, *531*, 504–508. [[CrossRef](#)]
24. Chen, R.; Huang, Y.C.; Gupta, S.; Lin, A.C.; Sanchez, E.; Kim, Y.; Saraswat, K.C.; Kamins, T.I.; Harris, J.S. Material characterization of high Sn-content, compressively-strained GeSn epitaxial films after rapid thermal processing. *J. Cryst. Growth* **2013**, *365*, 29–34. [[CrossRef](#)]

25. Trumbore, F.A. Solid Solubilities and Electrical Properties of Tin in Germanium Single Crystals. *J. Electrochem. Soc.* **1956**, *103*, 597–600. [[CrossRef](#)]
26. Zheng, J.; Li, L.; Zhou, T.; Zuo, Y.; Li, C.; Cheng, B.; Wang, Q. Growth of Crystalline Ge_{1-x}Sn_x Films on Si (100) by Magnetron Sputtering. *ECS Solid State Lett.* **2014**, *3*, 111–113. [[CrossRef](#)]
27. Rathore, J.; Nanwani, A.; Mukherjee, S.; Das, S.; Moutanabbir, O.; Mahapatra, S. Composition uniformity and large degree of strain relaxation in MBE-grown thick GeSn epitaxial layers, containing 16% Sn. *J. Phys. D Appl. Phys.* **2021**, *54*, 185105. [[CrossRef](#)]
28. Wei, L.; Miao, Y.; Pan, R.; Zhang, W.W.; Li, C.; Lu, H.; Chen, Y.F. Highly strained Ge_{1-x}Sn_x alloy films with high Sn compositions grown by MBE. *J. Cryst. Growth* **2021**, *557*, 125996. [[CrossRef](#)]
29. Wan, F.S.; Xu, C.; Wang, X.Y.; Xu, G.Y.; Cheng, B.W.; Xue, C.L. Study of strain evolution mechanism in Ge_{1-x}Sn_x materials grown by low temperature molecular beam epitaxy. *J. Cryst. Growth* **2022**, *577*, 126399. [[CrossRef](#)]
30. Olorunsola, O.; Said, A.; Ojo, S.; Abernathy, G.; Saha, S.; Wangila, E.; Grant, J.; Stanchu, H.; Acharya, S.; Du, W.; et al. Enhanced carrier collection efficiency of GeSn single quantum well towards all-group-IV photonics applications. *J. Phys. D Appl. Phys.* **2022**, *55*, 305101. [[CrossRef](#)]
31. Kong, Z.Z.; Wang, G.L.; Liang, R.R.; Su, J.L.; Xun, M.; Miao, Y.H.; Gu, S.H.; Li, J.J.; Cao, K.H.; Lin, H.X.; et al. Growth and Strain Modulation of GeSn Alloys for Photonic and Electronic Applications. *Nanomaterials* **2022**, *12*, 981. [[CrossRef](#)] [[PubMed](#)]
32. Grant, J.; Abernathy, G.; Olorunsola, O.; Ojo, S.; Amoah, S.; Wanglia, E.; Saha, S.K.; Sabbar, A.; Du, W.; Alher, M.; et al. Growth of Pseudomorphic GeSn at Low Pressure with Sn Composition of 16.7%. *Materials* **2021**, *14*, 7637. [[CrossRef](#)] [[PubMed](#)]
33. Tsukamoto, T.; Hirose, N.; Kasamatsu, A.; Matsui, T.; Suda, Y. Effects of Low-Temperature GeSn Buffer Layers on Sn Surface Segregation During GeSn Epitaxial Growth. *Electron. Mater. Lett.* **2020**, *16*, 9–13. [[CrossRef](#)]
34. Khelidj, H.; Portavoce, A.; Bertoglio, M.; Descoins, M.; Patout, L.; Hoummada, K.; Hallén, A.; Charai, A.; Benoudia, M.C.; Mangelinck, D. Ge(Sn) growth on Si(001) by magnetron sputtering. *Mater. Today Commun.* **2021**, *26*, 101915. [[CrossRef](#)]
35. Liu, X.Q.; Zheng, J.; Li, M.M.; Wan, F.S.; Niu, C.Q.; Liu, Z.; Zuo, Y.H.; Xue, C.L.; Cheng, B.W. Growth of relaxed GeSn film with high Sn content via Sn component-grade buffer layer structure. *J. Phys. D Appl. Phys.* **2021**, *54*, 435101. [[CrossRef](#)]
36. Abdi, S.; Assali, S.; Atalla, M.R.M.; Koelling, S.; Warrender, J.M.; Moutanabbir, O. Recrystallization and interdiffusion processes in laser-annealed strain-relaxed metastable Ge_{0.89}Sn_{0.11}. *J. Appl. Phys.* **2022**, *131*, 105304. [[CrossRef](#)]
37. Oka, H.; Mizubayashi, W.; Ishikawa, Y.; Uchida, N.; Mori, T.; Endo, K. Non-equilibrium solid-phase growth of amorphous GeSn layer on Ge-on-insulator wafer induced by flash lamp annealing. *Appl. Phys. Express* **2021**, *14*, 025505. [[CrossRef](#)]
38. Cai, H.J.; Qian, K.; An, Y.Y.; Lin, G.Y.; Wu, S.S.; Ding, H.K.; Huang, W.; Chen, S.Y.; Wang, J.Y.; Li, C. Thickness-dependent behavior of strain relaxation and Sn segregation of GeSn epilayer during rapid thermal annealing. *J. Alloys Compd.* **2022**, *904*, 164068. [[CrossRef](#)]
39. Wang, W.; Zhou, Q.; Dong, Y.; Tok, E.S.; Yeo, Y.-C. Critical thickness for strain relaxation of Ge_{1-x}Sn_x ($x \leq 0.17$) grown by molecular beam epitaxy on Ge(001). *Appl. Phys. Lett.* **2015**, *106*, 232106. [[CrossRef](#)]
40. Lin, K.C.; Huang, P.R.; Li, H.; Cheng, H.H.; Chang, G.E. Temperature-dependent characteristics of GeSn/Ge multiple-quantum-well photoconductors on silicon. *Opt. Lett.* **2021**, *46*, 3604–3607. [[CrossRef](#)]
41. Assali, S.; Nicolas, J.; Moutanabbir, O. Enhanced Sn incorporation in GeSn epitaxial semiconductors via strain relaxation. *J. Appl. Phys.* **2019**, *125*, 025304. [[CrossRef](#)]
42. Dou, W.; Benamara, M.; Mosleh, A.; Margetis, J.; Grant, P.; Zhou, Y.Y.; Al-Kabi, S.; Du, W.; Tolle, J.; Li, B.H.; et al. Investigation of GeSn Strain Relaxation and Spontaneous Composition Gradient for Low-Defect and High-Sn Alloy Growth. *Sci. Rep.* **2018**, *8*, 5640. [[CrossRef](#)] [[PubMed](#)]
43. Joe, M.; Yu, S.-Q.; Nupur, B.; Li, B.H.; Du, W.; John, T. Strain engineering in epitaxial Ge_{1-x}Sn_x: A path towards low-defect and high Sn-content layers. *Semicond. Sci. Technol.* **2017**, *32*, 124006.
44. Zheng, J.; Liu, Z.; Zhang, Y.W.; Zuo, Y.H.; Li, C.B.; Xue, C.L.; Cheng, B.W.; Wang, Q.M. Growth of high-Sn content (28%) GeSn alloy films by sputtering epitaxy. *J. Cryst. Growth* **2018**, *492*, 29–34. [[CrossRef](#)]
45. Dev, S.; Kiangte, K.R.; Lodha, S. Wafer-scale mono-crystalline GeSn alloy on Ge by sputtering and solid phase epitaxy. *J. Phys. D-Appl. Phys.* **2020**, *53*, 21LT01. [[CrossRef](#)]
46. Qian, L.; Tong, J.C.; Suo, F.; Liu, L.; Fan, W.J.; Luo, Y.; Zhang, D.H. GeSn/GaAs Hetero-Structure by Magnetron Sputtering. *IEEE J. Quantum Electron.* **2020**, *56*, 1–5. [[CrossRef](#)]
47. Abdel-Rahman, M.; Alduraibi, M.; Hezam, M.; Ilahi, B. Sputter deposited GeSn alloy: A candidate material for temperature sensing layers in uncooled microbolometers. *Infrared Phys. Technol.* **2019**, *97*, 376–380. [[CrossRef](#)]
48. Zhang, L.; Wang, Y.S.; Chen, N.L.; Lin, G.Y.; Li, C.; Huang, W.; Chen, S.Y.; Xu, J.F.; Wang, J.Y. Raman scattering study of amorphous GeSn films and their crystallization on Si substrates. *J. Non-Cryst. Solids* **2016**, *448*, 74–78. [[CrossRef](#)]
49. Tsukamoto, T.; Hirose, N.; Kasamatsu, A.; Mimura, T.; Matsui, T.; Suda, Y. Formation of GeSn layers on Si (001) substrates at high growth temperature and high deposition rate by sputter epitaxy method. *J. Mater. Sci.* **2015**, *50*, 4366–4370. [[CrossRef](#)]
50. Miao, Y.H.; Wang, Y.B.; Hu, H.Y.; Liu, X.Y.; Su, H.; Zhang, J.; Yang, J.Y.; Tang, Z.H.; Wu, X.; Song, J.J.; et al. Characterization of crystalline GeSn layer on tensile-strained Ge buffer deposited by magnetron sputtering. *Mater. Sci. Semicond. Process.* **2018**, *85*, 134–140. [[CrossRef](#)]
51. Gencarelli, F.; Vincent, B.; Demeulemeester, J.; Vantomme, A.; Moussa, A.; Franquet, A.; Kumar, A.; Bender, H.; Meersschant, J.; Vandervorst, W.; et al. Crystalline Properties and Strain Relaxation Mechanism of CVD Grown GeSn. *ECS J. Solid State Sci. Technol.* **2013**, *2*, P134–P137. [[CrossRef](#)]

-
52. D'Costa, V.R.; Tolle, J.; Roucka, R.; Poweleit, C.D.; Kouvetakis, J.; Menéndez, J. Raman scattering in Ge_{1-y}Sn_y alloys. *Solid State Commun.* **2007**, *144*, 240–244. [[CrossRef](#)]
 53. Su, S.; Wang, W.; Cheng, B.W.; Hu, W.X.; Zhang, G.Z.; Xue, C.L.; Zuo, Y.H.; Wang, Q.M. The contributions of composition and strain to the phonon shift in alloys. *Solid State Commun.* **2011**, *151*, 647–650. [[CrossRef](#)]